Improving the detection efficiency and modulation transfer function of lens-coupled indirect X-ray imaging detectors based on point spread functions simulated according to lens performance parameters

Yanping Wang,[a,b] Gang Li,[a,c]* Jie Zhang,[a] Qiru Yi,[b,c] Yue Zhao,[a,b] Kun Li,[a,b] Ye Zhu[a,b] and Xiaoming Jiang[a,c]*

[a]Institute of High Energy Physics, Chinese Academy of Science, Yuquan Road 19B, Shijingshan District, Beijing 100049, People's Republic of China, [b]University of Chinese Academy of Sciences, Yuquan Road 19A, Shijingshan District, Beijing 100049, People's Republic of China, and [c]Beijing Advanced Sciences and Innovation Center of CAS, Chinese Academy of Science, Yanqi South Fourth Street, No. 26, Huairou District, Beijing 101047, People's Republic of China. *Correspondence e-mail: lig@ihep.ac.cn, jiangxm@ihep.ac.cn

Lens-coupled indirect X-ray imaging detectors have the advantage of high resolution and the disadvantage of low detection efficiency. Using thicker single-crystalline films (SCFs) can improve the detection efficiency. However, the image quality will become worse due to the degradation of the point spread function (PSF) and modulation transfer function (MTF). This disadvantage can be improved by deconvolution with the PSF, which is unknown. In this article, a method was established to acquire the PSF based on a simulation of the imaging process for a lens-coupled indirect X-ray imaging detector. Because the structural parameters of commercial lenses cannot usually be obtained, the PSFs were calculated from lens performance parameters. PSFs were calculated using the conditions of 12 keV X-ray energy, 10× and 40× magnification objectives and 4.6 µm- and 20 µm-thick GGG:Tb scintillators. These were then used to deconvolve images of an Xradia resolution test pattern taken under the same conditions. The results show that after deconvolution the MTF had been clearly improved for both the 4.6 µm- and 20 µm-thick SCFs, indicating that the image has better quality than before deconvolution. Furthermore, a PSF deconvolution was performed on mouse brain tissue projection images, and the original and deconvolution projection images were used to perform computed-tomography reconstruction; the result proved that the method was effective for improving the image quality of low-contrast samples. Therefore, this method shows promise in allowing the use of thick SCFs to improve the detection efficiency while maintaining good image quality.

1. Introduction

X-ray non-destructive imaging is one of the three main synchrotron radiation techniques for studying the properties of matter (imaging, diffraction and spectroscopy). To fully exploit synchrotron radiation in non-destructive imaging applications, high-performance detectors are required. Among the available types of detectors, lens-coupled X-ray indirect imaging detectors can achieve resolutions in the submicrometre to several micrometres range, making them a very important detection tool in the fields of materials, biomedicine and fossils (Gruner, 2012). These detectors are mainly composed of a scintillation crystal, a lens-coupled system (objective, tube lens and eyepiece) and a camera (see
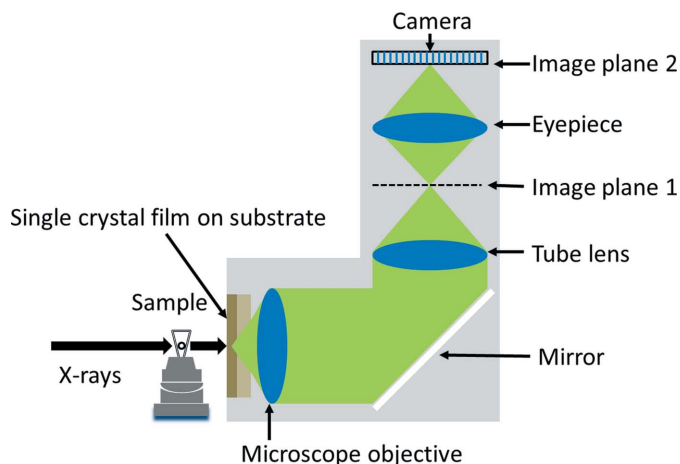
Figure 1
Imaging schematic illustration of the lens-coupled indirect X-ray imaging detector.

Fig. 1). Scintillation crystals are responsible for the conversion of X-ray images into visible-light images. The currently widely used scintillation crystals are single-crystalline films (SCFs) (Cecilia *et al.*, 2011, 2014). This is because SCFs have the following excellent properties. First, the perfect SCF has no grain boundaries inside the single crystal, so it can reduce the scattering of both the X-rays and visible light. Second, when the X-ray energy is low, the photoelectric effect is the main mode of interaction between the X-rays and the SCF. Compton scattering and Rayleigh scattering are weak and almost negligible. Third, the radial extent of electron propagation is only hundreds of nanometres within the SCFs (Hoheisel *et al.*, 2004; Martin & Koch, 2006). This is much smaller than the effective pixel size of the detector (camera pixel size divided by the lens total magnification), and, coupled with the fact that the percentage of energy deposition also rapidly decreases within this distance, the radial expansion of the visible light from the emission point can be neglected (Koch *et al.*, 1998). In summary, the original propagation direction of the X-rays is unchanged within the SCF, and the emission of the visible light only takes place where X-ray photons pass. These excellent features ensure that the detector has a high spatial resolution. The objective lens and the tube lens form an infinitely conjugate optical path, they are responsible for enlarging the visible images in the SCF to the image plane 1, and the mirror is responsible for changing the propagation direction of the visible light and preventing radiation damage to the camera. The eyepiece is responsible for magnifying the images on image plane 1 to make the detector satisfy Nyquist's law, which enables the detector to observe the diffraction resolution limit of the lens system. The camera is responsible for receiving and storing the enlarged images. In short, the detector imaging process is as follows: the SCF converts the normal-incidence X-ray intensity into visible-light images which are generated at different depths inside the SCF, and then the lens-coupled system enlarges the visible-light images and projects them onto the camera (Douissard *et al.*, 2010).

Lens-coupled X-ray indirect imaging detectors have the advantage of high resolution compared with flat-panel imaging detectors and fibre-coupled X-ray imaging detectors (Uesugi *et al.*, 2011), but have the disadvantage of a relatively low detection efficiency. To improve the detection efficiency of the detector, the following perspectives can be considered: (i) use a camera with high photoelectric conversion efficiency; (ii) design lens-coupled systems with high visible-light transmission and high numerical aperture (NA); (iii) use SCFs with high X-ray absorption and high X-ray conversion efficiency; and (iv) increase the thickness of the SCF. At present, CCD and sCMOS are usually used as visible-light cameras (Smith, 2011), and their quantum efficiency has reached more than 90% at some wavelengths (Bebek *et al.*, 2012, 2017). At some visible wavelengths, the transmittance of commercial optical systems is as high as 80% (Manoochehri & Ikonen, 1995; Rahmani *et al.*, 2014). The NA of lens-coupled systems has also been greatly optimized under the condition of small aberrations in the lens-coupled system and sufficient working distance for SCFs. Therefore, the potential of increasing the detection efficiency from the first two approaches has been very limited. In order to improve the ability of SCFs to absorb and convert X-rays, many research institutes have carried out extensive research and have developed many new types of SCFs for detectors (Khartsev & Grishin, 2005a,b; Martin *et al.*, 2009; Douissard *et al.*, 2010; Zorenko *et al.*, 2014). Increasing the thickness of the SCF can further improve the detection efficiency but will disperse the PSF and decrease the modulation transfer function (MTF) (Zorenko *et al.*, 2010; Cecilia *et al.*, 2011). The main reason for this is the limition of the depth of field (DOF) of the lens system and camera. The formula to describe the DOF is shown in formula (1),

$$d_{\text{tot}} = \frac{n_{\text{air}}\,\lambda}{\text{NA}^2} + \frac{n_{\text{air}}\,e}{M\,\text{NA}}, \qquad (1)$$

where d_{tot} represents the DOF, λ is the wavelength of the visible light emitted by the SCF, n_{air} is the refractive index of air, NA is the objective numerical aperture, the variable e is the camera's pixel size and M is the magnification of the lens system (Kenneth & Michael, 2017). For high-resolution microscopy imaging systems, the calculated DOF using formula (1) is only a few micrometres. Therefore, when the thickness of the SCF is matched to the DOF of the lens and camera, good image quality can be achieved. However, formula (1) does not consider the refraction of visible-light photons by the SCF. In fact, although the thickness of the SCF is smaller than the DOF, the image will still be blurred. Hence, no matter how thick the SCF is, the detector always produces blurred images. It is known that deconvolution algorithms can improve image quality. Therefore, there is a potential for using a thicker SCF to improve the detection efficiency while maintaining good image quality. In order to obtain relatively clear images from the blurred images, research on image restoration technology for a lens-coupled X-ray indirect imaging detector has been previously carried out where a Gaussian function was used to simulate the PSF of the detector system, and the projection to a convex set algorithm

was then used to deconvolve the simulated images (Li *et al.*, 2015). A second method using blind deconvolution and dark channel prior technology to obtain high-contrast images has also been used (Wang *et al.*, 2015). Generally speaking, knowledge of the detector PSF can theoretically explain the process of image blurring and result in better image quality. However, the actual PSF of the detector is difficult to obtain for the following reasons: first, the structural parameters (lens material, thickness, radius of curvature and so on) of the commercial lens system are difficult to obtain, which makes it difficult to analyse the PSF of the detector system by optical software; second, it is also difficult to experimentally obtain a PSF due to experimental equipment limitations and system noise effects. Therefore, further studies of methods to obtain a relatively accurate PSF for the detector will be important.

In this article, we describe a geometric optical imaging method that simulates the PSF of a lens-coupled X-ray imaging detector during the focusing process using the performance parameters of the system (lens focal length, aperture size, *etc.*) which can be measured by laboratory tools. To verify the viability of the proposed PSF method, this method was applied to the detector system developed by Beijing Synchrotron Radiation Facility (BSRF). Under conditions of 12 keV X-ray energy, 10× and 40× magnification objectives and 4.6 µm- and 20 µm-thick GGG:Tb scintillators, the respective PSFs were simulated and then used to deconvolve the Xradia resolution test pattern's images which were taken under the same conditions. The results show that, after deconvolution, the MTF had been clearly improved for both the both 4.6 µm- and 20 µm-thick SCFs, showing that the image has better quality than before. Additionally, the method proposed in this article was used in mouse brain tissue projection imaging. The deconvolved image and CT reconstruction image were of better quality than the original results, which confirmed the validity and generality of the proposed method. Therefore, the method to simulate the PSFs of the detector has been shown to be practical and shows promise in using thicker SCFs to improve the detection efficiency while maintaining good image quality.

2. Imaging principle and modelling

2.1. Imaging principle

Since the divergence of synchrotron radiation is very small, the X-rays can be approximated as parallel light. After passing through the sample, the X-rays will carry the sample's information; they are perpendicularly incident on the SCF. Since the SCF has a certain thickness, X-ray intensities absorbed at different depths of the SCF are different. Generally speaking, as the depth increases, the number of absorbed X-rays will decline. Furthermore, it is clear that the intensity of the visible light emitted by each layer of the SCF is directly proportional to the intensity of the absorbed X-rays. Therefore, the visible-light intensity will decline as the depth increases (see Fig. 2). When the lens-coupled system transfers the visible-light images to the camera, the visible-light image at the same depth

will be modulated by the same PSF (Bamieh *et al.*, 2002). Visible-light images at different depths will be modulated by different PSFs. These modulated visible-light images are projected onto the camera. Then the general mathematical expression for the detector's imaging function can be expressed by formula (2),

$$\begin{aligned}
g(x,y) &= \int_{z_1}^{z_2} [k(z)f(x,y)] * \mathrm{PSF}(x,y,z)\,\mathrm{d}z \\
&= \int_{z_1}^{z_2} f(x,y) * [k(z)\,\mathrm{PSF}(x,y,z)]\,\mathrm{d}z \\
&= f(x,y) * \int_{z_1}^{z_2} [k(z)\,\mathrm{PSF}(x,y,z)]\,\mathrm{d}z \\
&= f(x,y) * \left[K\,\mathrm{PSF}_{\mathrm{total}}(x,y)\right] \\
&= [Kf(x,y)] * \mathrm{PSF}_{\mathrm{total}}(x,y),
\end{aligned} \qquad (2)$$

where $*$ represents the convolution symbol, z_1 is the distance from the left side of the SCF to the focal plane of the objective, z_2 is the distance from the right side of the SCF to the focal plane of the objective, $z_2 - z_1$ is the thickness of the SCF, $\mathrm{PSF}(x,y,z)$ is the normalized PSF at position z, $k(z)f(x,y)$ is the geometrical optical ideal image of the visible-light image at position z, $k(z)$ indicates the difference in intensity at different depth positions, k is the sum of $k(z)$ after passing through the lens system, and $\mathrm{PSF}_{\mathrm{total}}(x,y)$ is the detector's normalized PSF (Li *et al.*, 2015).

Derived from formula (2), the PSF of the detector can be expressed as formula (3),

$$\mathrm{PSF}_{\mathrm{total}}(x,y) = (1/K) \int_{z_1}^{z_2} [k(z)\,\mathrm{PSF}(x,y,z)]\,\mathrm{d}z. \qquad (3)$$

To summarize formula (3), $\mathrm{PSF}_{\mathrm{total}}(x,y)$ can be obtained by integrating the individual PSFs from different depths as the X-rays penetrate into the SCF. In an actual experiment, prior to imaging a sample, the distance between the SCF and the
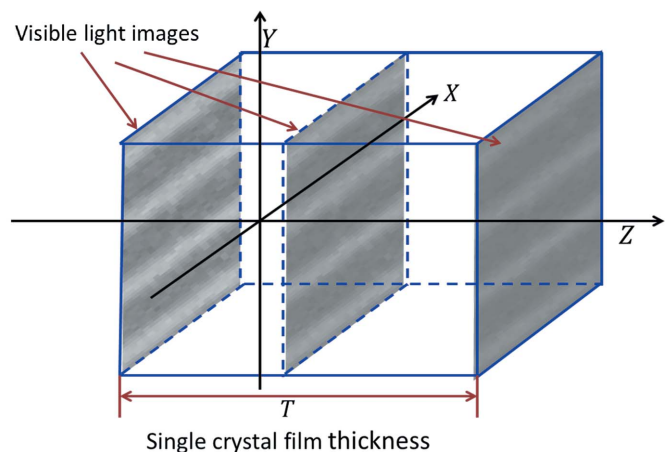

Figure 2
Intensity distribution of visible-light images at different depth positions of the SCF. The images at the different positions have the same structural information but different intensities. The intensity of the visible-light image decreases as depth increases.

objective needs to be varied in order to find the best imaging position, because the detector's normalized PSF will change as the distance between the SCF and the objective changes. Therefore, it is necessary to simulate the PSFs during the focusing process to optimize the system.

2.2. Modelling

2.2.1. Geometric optical imaging diagram. Fig. 1 shows the configuration of the detector system. For the convenience of simulation, the 45° mirror was removed from the geometrical optical path (see Fig. 3), allowing all the optics to be placed on the main optical axis of the objective lens. The effect of eyepiece aberration on imaging quality was also ignored. Thus, by considering the camera and eyepiece as a single unit, this unit becomes an effective camera placed at the location labelled 'Image plane 1' with an effective pixel size equal to the camera's pixel size divided by the magnification of the eyepiece. At the same time, a three-dimensional Cartesian coordinate system was established, the Z axis is along the main optical axis, the X axis is parallel to the detector's row pixels, the Y axis is parallel to the detector's column pixels, and the origin coordinate A_2 is on the focal point of the objective. Before the PSFs of the detector are simulated, as in Fig. 3, the SCF needs to be discretized and the performance parameters of the lens-coupled system need to be measured.

Firstly, the SCF was discretized along the Z axis, as shown in Fig. 4. The SCF's thickness T, in steps of ΔT, was divided into
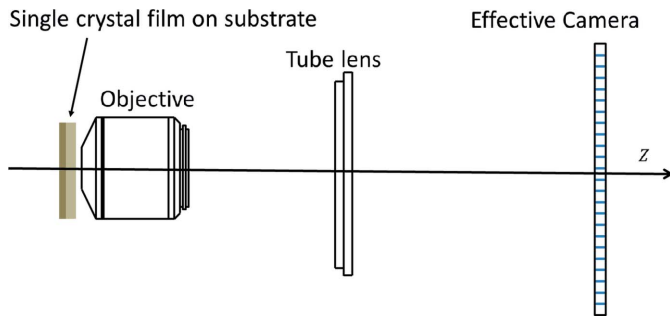

Figure 3
Simplified diagram of the lens-coupled X-ray indirect imaging detector in the XZ or YZ section. Compared with Fig. 1, the 45° mirror was removed and the eyepiece was combined with the camera as an effective camera.
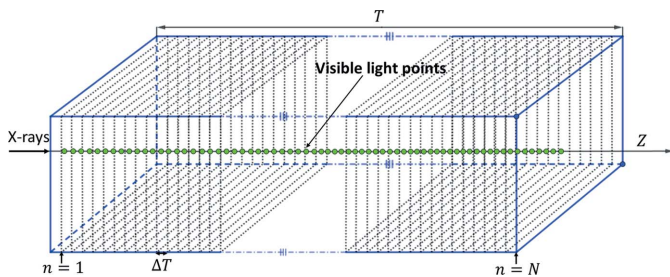

Figure 4
Schematic of the visible-light points in a single X-ray path. The SCF thickness T was divided into N layers in steps of ΔT. Visible-light spots were generated on the last plane of each layer.

N parts. A single X-ray with an intensity I_0 is incident along the Z axis. The linear absorption coefficient of the SCF to X-rays is ρ. According to the law of absorption (McKetty, 1998), the X-ray intensity absorbed in the first ΔT is $I_0[1 - \exp(-\rho\Delta T)]$, the second ΔT is $I_0 \exp(-\rho\Delta T)$ $[1 - \exp(-\rho\Delta T)]$, the third ΔT is $I_0 \exp(-2\rho\Delta T)$ $[1 - \exp(-\rho\Delta T)]$, and the nth ΔT is $I_0 \exp[-(n-1)\rho\Delta T]$ $[1 - \exp(-\rho\Delta T)]$. Therefore, it is easy to find the ratio of X-ray intensity absorbed by each layer. Because ΔT is very small, we can assume that the X-rays are absorbed on the last plane of ΔT. Since the absorption of the X-ray intensity of each layer is proportional to the visible-light intensity emitted at each point, the ratio of the visible-light intensity emitted from each layer is obtained as shown in formula (4),

$$k_1 : k_2 : k_3 : \ldots : k_N = 1 : \left[\exp(-\rho\Delta T)\right]^1 : \left[\exp(-\rho\Delta T)\right]^2$$
$$: \left[\exp(-\rho\Delta T)\right]^3 : \ldots$$
$$: \left[\exp(-\rho\Delta T)\right]^{N-1}. \quad (4)$$

Therefore, the PSFs of the detector's discrete expression can be shown as formula (5),

$$\text{PSF}_{\text{total}}(x, y) = (1/K) \sum_{i=1}^{i=N} k_i \, \text{PSF}_i(x, y, z_i) \quad (5)$$

$$= (1/K) \sum_{i=1}^{i=N} \left[\exp(-\rho\Delta T)\right]^{N-1} \text{PSF}_i(x, y, z_i).$$

Secondly, lens performance parameters can be measured according to the configuration of the lens-coupled system. The performance parameters mainly include the objective lens focal length, working distance, the first and the last piece of the objective's diameter, the position of the objective's object principal plane and image principal plane, the distance between the object principal plane and the image principal plane, the distance between the objective and tube lens, tube lens diameter and focal length, and the distance between the tube lens and the effective camera. According to the measured performance parameters, a geometrical diagram of the lens system is shown in Fig. 5. In the figure, A_2 and F_1 are the object focus point and image focus point of the objective, and B_1B_3 and C_1C_3 are the diameters of the first glass and the last glass of the objective. $H_{14}H_{15}$ and $H_{24}H_{25}$ are the position of objective's object principal plane and image principal planes. $H_{12}H_{22}$ is the distance between the two principal planes. C_2A_2 is the par-focal distance of the objective, and Q_1Q_3 is the tube lens diameter. C_2Q_2 is the distance between objective and tube lens, P_1P_3 is the position of effective camera, and Q_2P_2 is the tube lens image focal length.

Fig. 5 shows a schematic of the lens-coupled system imaging the visible light emitted from the points in Fig. 4. On the basis of Fig. 5, we will use our simulation method to image the emitted visible-light points onto the effective camera. Before obtaining the simulation results, it is important to know how the photons propagate in the detector. The photon's propagation rules in the detector are as follows:

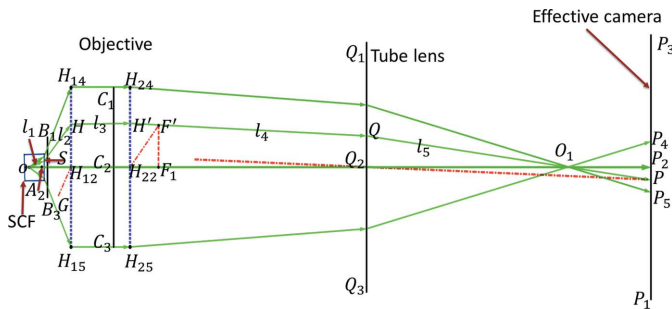(i) Find a luminous point O in the SCF (see Figs. 5 and 6). The photons emitted by the luminous spot O are equally

Figure 5
Geometry imaging model of the detector. A_2 and F_1 are the object focus point and image focus point of the objective, B_1B_3 and C_1C_3 are the diameters of the first glass and the last glass of the objective. $H_{14}H_{15}$ and $H_{24}H_{25}$ are the position of the objective's object principal plane and image principal plane. $H_{12}H_{22}$ is the distance of the two principal plane. C_2A_2 is the par-focal distance of the objective lens, and Q_1Q_3 is the tube lens diameter. C_2Q_2 is the distance between the objective and tube lens, P_1P_3 is the position of the effective camera, and Q_2P_2 is the tube lens image focal length. Point O is one of the luminous points inside the SCF along the Z axis. O_1 is the image of the point O.

probable within a 4π solid angle. Taking one of the photons as an example, the propagation direction for the photon can be expressed by θ which is the angle between the positive direction of the photon and the positive Z axis, and φ is the angle between the projection of the positive direction of the photon on the XY plane and the positive direction of the X axis. The photon's direction vector is expressed mathematically as formula (6),

$$n_1 = \left(\sin\theta\cos\varphi, \sin\theta\sin\varphi, \cos\theta\right), \tag{6}$$

where $\theta \in [-\pi/2, \pi/2]$, $\varphi \in [0, 2\pi)$. In order to speed up the simulation process, the range of θ can be taken as $(0, \pi/2]$. Then the photon will intersect the left side of the substrate at point $S(x_S, y_S, z_S)$. According to n_1 and point coordinates O
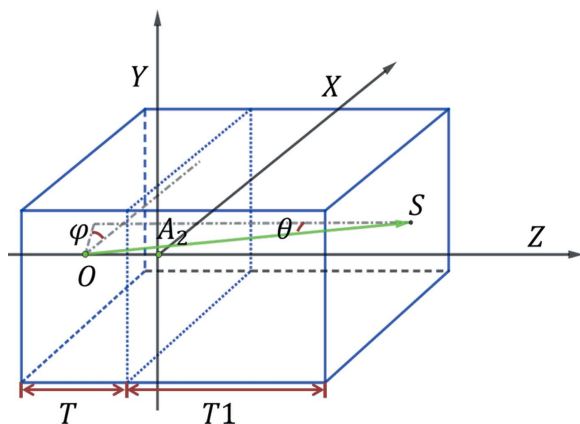

Figure 6
Schematic of the propagation direction of a photon in the SCF. O is one of the visible-light spots in the SCF. It emits visible photons with equal probability within a 4π solid angle. OS is the direction of photon propagation. Whereas φ is the angle between the projection of OS on the XY plane and the positive direction of the X axis, θ is the angle between the positive direction of OS and the positive direction of the Z axis. T is the thickness of the SCF, and $T1$ is the substrate thickness.

we can obtain a three-dimensional linear equation l_1 and S point coordinates.

(ii) According to the refraction law, the SCF's normal vector $\mathbf{n}_0 = (0, 0, 1)$, equation l_1 and S point coordinates, the linear equation of refracted light l_2 can be calculated. Then we can obtain the intersection coordinates $H(x_H, y_H, z_H)$ between the linear equation l_2 and the object principal plane. After judging whether or not the condition $x_H^2 + y_H^2 \le (H_{14}H_{12}/2)^2$ is true, if true the photon continues to propagate. When the photon propagates between the two principal planes, its propagation direction is $(0, 0, 1)$. Therefore, it can be very simple to determine the intersection coordinates $H' = [x_{H'}, y_{H'}, z_{H'}]$ of the straight line l_3 and the image principal plane.

(iii) Next, to find the propagation direction of the photon after the H' point, draw a straight line GH_{12} parallel to the straight line l_2. Suppose another photon travels along the straight line GH_{12}; then the photon will propagate in the same direction at point H_{22}, and we can obtain the coordinate F' between the photon and the image focal plane. Based on optical principles we can know if $H'F'$ is the first photon's propagation direction (Ajoy, 2008). According to H', F' and the position of tube lens, we obtain the three-dimensional linear equation l_4 and Q point coordinates. After judging whether or not the condition $x_Q^2 + y_Q^2 \le (Q_1Q_3/2)^2$ is true, if true the photon continues to propagate.

(iv) After the photon passes point Q, the way to determine the photon's propagation direction l_5 is the same as the third step, so the search process is omitted here. According to l_5, the Q point and the position of the effective camera, we can obtain the position P where the photon falls on the effective camera. Finally, we determine which pixel has been struck by the photon. All the visible photons in the SCF are transmitted as described above. When describing the propagation rules, the objective's main planes are considered as an aperture stop. If the first glass or the last glass of the objective is an aperture stop, the corresponding criterion should be added to limit the propagation direction of the photons. After all the photons have been transmitted, we can obtain the image of the spots on the effective camera. Then, once the image is normalized, the detector's PSF will be obtained. The above method is applicable regardless of the distance between the SCF and the objective. In order to find the position that provides the best PSF, a scan of the distance between the objective and the SCF is performed. At each object distance, the above method is used to obtain the corresponding PSF of the detector. This can also be regarded as the evaluation of the PSFs in the focusing process.

2.2.2. Simulation PSF. As an example, the detector developed by BSRF has been used to study the simulation of the PSF. The configuration of the detector is as follows: the GGG:Tb thicknesses are 4.6 μm and 20 μm, respectively, and they were both grown on 170 μm-thick GGG. The objective magnifications are 10× and 40×, respectively. The parameters of the two objectives are shown in Table 1. The diameter of the tube lens is 250 mm and its focal length is 180 mm. The distance between the tube lens and objective lens is 160 mm. The magnification of the eyepiece is 3.3×. The CCD type is

Table 1
Performance parameters of the two objectives.

Amplification factor	NA	First glass diameter (mm)	Last glass diameter (mm)	Object focal length (mm)	Working distance (mm)	Distance of the two principal planes (mm)	Parfocal distance (mm)
10×	0.4	6	16	18	3.1	37.3	45
40×	0.6	7	6.8	4.5	2.7	40.0	45

iXon Ultra 888 (Andor), the number of pixels is 1024 × 1024, and the physical pixel size is 13 μm × 13 μm. From the number of objectives and SCFs, the detector has four conditions. When using a computer to simulate the PSFs of the four conditions, the X-ray energy was taken as 12 keV. The visible wavelengths produced by the GGG:Tb are around 550 nm. Ignoring the other wavelengths of visible light, we only used a single wavelength of 550 nm (Martin *et al.*, 2010). The refractive index of GGG:Tb for 550 nm visible light was calculated to be 1.937 (He & Guan, 1985) and the linear absorption coefficient ρ of GGG:Tb for 12 keV X-rays is about 0.1085 μm^{-1}. When the SCFs were discretized, ΔT was taken as 0.1 μm and the number of visible photons emitted by the first layer of the SCFs was 10^{10}. According to formula (4), the number of photons generated by the other layers can also be calculated. Fig. 7 shows the relative difference in the number of visible photons which are produced by each layer. It can be seen, as the depth increases, that the number of visible photons produced by each layer rapidly decreases.

According to parameters of the four detectors and the method in §2.2.1, the PSFs during the focusing process can be obtained. For any detector the following steps should be performed. First, place the left-most SCF 100 μm to the left of the objective focal point (see Fig. 5). Second, image the visible-light spots emitted from all the layers in the SCF. Third, normalize the image of the visible spots and then the PSF of the detector corresponding to the position of the SCF can be obtained. Fourth, let the SCF move towards the objective with a step of 0.1 μm and, according to the second and third step, obtain the detector's PSF. Fifth, repeat the fourth, second and third steps until the leftmost SCF is 70 μm to the left of the objective focal point. Taking into account the movement per step, it can be seen that the SCF will have 301 positions when it moves in the range from −100 μm to −70 μm. As a result, there are 301 PSFs for the detector. In order to show the changes of the PSFs, schematics of *XZ* or *YZ* section PSFs for the four conditions are shown in Fig. 8. From Fig. 8 we can see the following: (i) for each condition, the PSF of the detector will change when the position of the SCF

changes; (ii) when using the same objective, the thicker the SCF, the more diffuse the PSF; (iii) when using the same thickness of SCF, the larger the objective magnification, the more pixels the PSF occupies.

Then, the PSFs and the ideal image convolution method were used to find the PSF with the best focus position from the 301 PSFs. The process is as follows. First, simulate an ideal image in object space with a spatial resolution of about 127 line-pairs mm^{-1} and a contrast ratio of 90.48% for 10× objective and an ideal image in object space with a spatial resolution of about 508 line-pairs mm^{-1} and a contrast ratio of
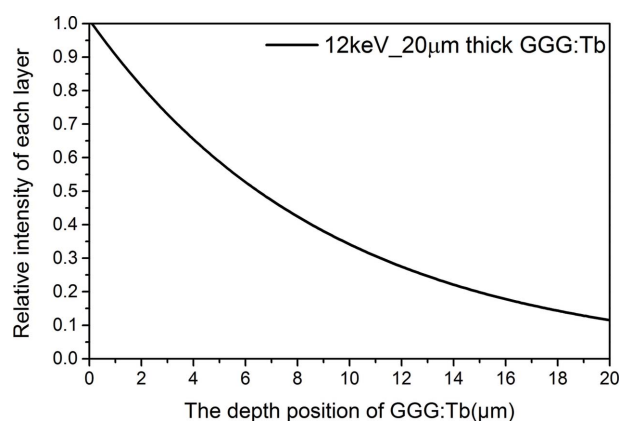

Figure 7
Schematic diagram showing the relative difference in the intensity of the visible-light spots which are produced by each luminous layer of GGG:Tb. It can be seen that, as the depth increases, the number of visible photons which are produced by each layer gradually decreases.
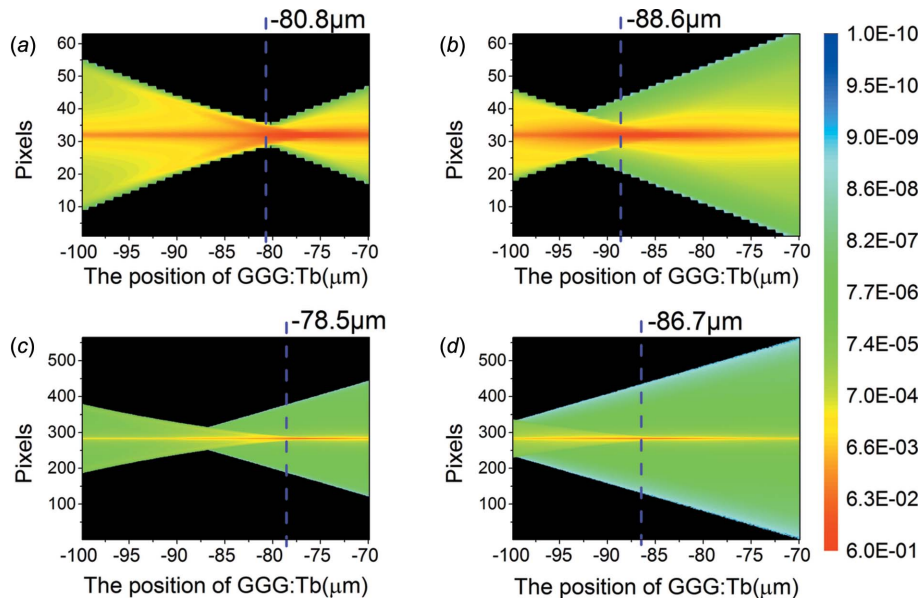

Figure 8
The changes of the detector's PSFs in the *XZ* or *YZ* section during the focusing process. The conditions corresponding to (*a*) are 10× objective, 4.6 μm-thick GGG:Tb; (*b*) are 10× objective, 20 μm-thick GGG:Tb; (*c*) are 10× objective, 4.6 μm-thick GGG:Tb; (*d*) are 10× objective, 20 μm-thick GGG:Tb. In each case, the position of the best-focus PSF is marked with a purple dashed line.
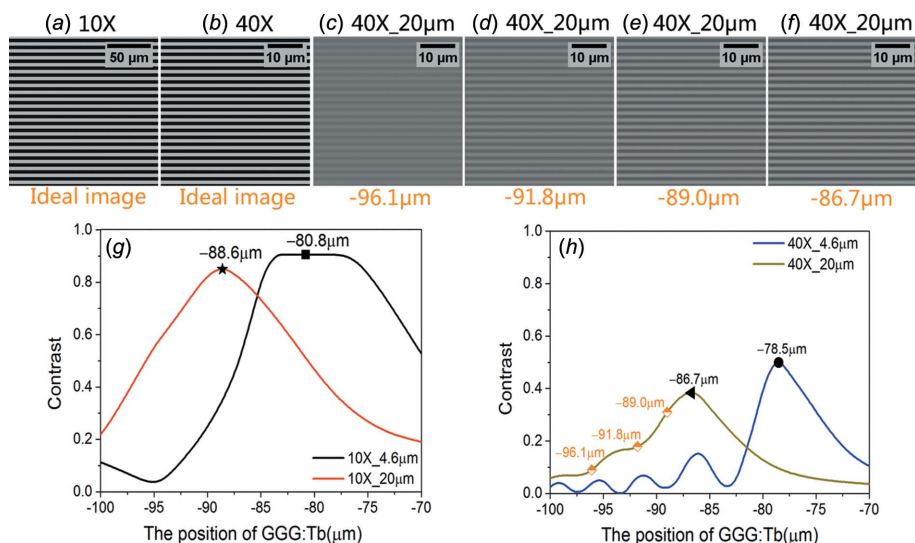
Figure 9
(a) Ideal image in object space with a spatial frequency of about 127 line-pairs mm^{-1} and a contrast of 90.48% for the 10× objective. (b) Ideal image in object space with a spatial frequency of about 508 line-pairs mm^{-1} and a contrast of 90.48% for the 40× objective. (g, h) Diagrams of the contrast in the blurred images after images (a) and (b) were convolved with the PSFs from Fig. 8. For each case there is a PSF that maximizes the contrast in the blurred images. We call this corresponding PSF the detector's best-focus PSF. The positions of the best focus were marked in the curves. (c)–(f) Blurred images which are simulated at the positions marked in (h) when the 40× objective was focused on a 20 μm-thick GGG:Tb. We can see that the blurred image in the best focus position has the best image quality.

90.48% for 40× objective (see Figs. 9a and 9b). Second, use the PSFs obtained from the focusing process to convolve with the respective ideal image. Third, compute the spatial contrast of the convolved images. Finally, find the position with the highest spatial contrast. Figs. 9(g) and 9(h) show the changes of the spatial contrast after the ideal image was convolved with the PSFs, and the positions of the largest contrasts which correspond to the best-focus PSFs are marked in the figure. At the same time, in order to demonstrate the changes of the image quality during the focusing process, Figs. 9(c)–9(f) show blurred images which were simulated at the positions marked in Fig. 9(h) when the 40× objective was focused on 20 μm-thick GGG:Tb. We can see that the images in the four positions are all blurred compared with the ideal image, and the image quality at the best focus position is relatively good.

In addition, from the positions of the best-focus PSFs marked in Fig. 8, we can find that the PSFs in the best focus positions are not the least diffuse, and the best focus positions from the origin A_2 are about −80 μm. In fact, we think (i) the best-focus PSF should be the least diffuse, and (ii) the best focus position should be around the origin A_2. The reason for (i) is that the intensity distribution of the best-focus PSF can give the blurred image a better contrast; the reason for (ii) is that the SCF has a 170 μm-thick substrate and we considered the refraction of the visible light between the scintillator and air. If we ignore the refraction, the best focus position is around the origin A_2. However, as Fig. 10 shows, after the photon is refracted, A' is the intersection of the reverse extension of the refracted ray with the main optical axis, the distance between point A' and the origin A_2 is 98.4 μm, and,

therefore, the rays from origin A_2 can be seen from point A'; in order to let A' point at the DOF of the lens and camera, the scintillator should be moved in the negative direction of the Z axis. Finally, the best-focus PSFs of the four conditions are displayed in Fig. 11. In order to better display the PSFs, we used a pseudocolor map and three-dimensional maps to draw the PSFs. As can be seen from Fig. 11, when the objective is the same, then the thicker the SCF, the more diffuse the best-focus PSF; when the SCF is the same, then the larger the objective magnification, the more diffuse the PSF.

3. Experiments and data processing

3.1. Experiments

An experimental study was conducted at the BSRF 4W1A beamline station; an X-ray energy of 12 keV was selected by two Si(111) crystals (Yuan *et al.*, 2007; Yi *et al.*, 2015). The experimental sample is an Xradia resolution test pattern manufactured by ZEISS (model X500-200-16) made from Au with 1.6 μm tall features. The horizontal and vertical pitches are from 1 μm to 16 μm, corresponding to spatial frequencies from 1000 line-pairs mm^{-1} to 62.5 line-pairs mm^{-1} that enable both resolution tests and MTF measurements. The other parameters of the detector are the
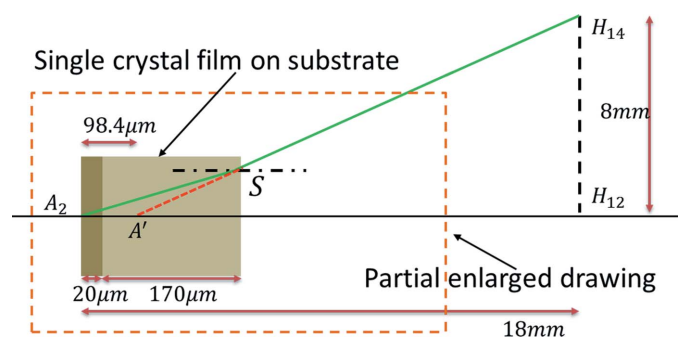

Figure 10
Refraction diagram of visible light between the scintillator and air. The thickness of the GGG:Tb is 20 μm, and the thickness of substrate GGG is 170 μm. The magnification of the objective is 10× (NA = 0.4). A photon from A_2 travels along A_2S and will refracted when it propagates to the interface of the scintillator with the air. The reverse extension line of the refracted light will intersect with the main optical axis at point A'. If the leftmost surface of the SCF is on the focal plane of the objective, the distance between point A_2 and point A' is about 98.40 μm. When the optical system is imaging an object at point A', the PSF of A' will spread widely. If the SCF was moved to the left by 70 or 80 μm, A' will be near the focal plane of the objective, then the PSF of A' will be less diffuse. This is the reason why the position of the SCFs is in the negative direction of the objectives focal points when the four best-focus PSFs were obtained.

Table 2
Experimental conditions for shooting X-ray images without samples.

Amplification factor	GGG:Tb thickness	Exposure time (s)	Value of ionization chamber	Average value of images without samples
10×	4.6 μm	200	7.60×10^{-8}	30091
10×	20 μm	80	6.31×10^{-8}	37337
40×	4.6 μm	240	9.05×10^{-8}	2141
40×	20 μm	240	6.30×10^{-8}	4500

same as in §2.2.2. In the experiment, the distances between the Xradia resolution test pattern and the SCFs were all 0.5 cm; the mechanical focusing step was set to 0.1 μm. In the focusing process the best focus position for each condition was found. At the best focus position, the incident X-rays were imaged with and without the Xradia resolution test pattern. For all the different measurement conditions, the value of the ionization chamber current and the average value of the image intensity without the sample are shown in Table 2. Figs. 12(A1)–12(D1) show images of the test pattern taken under different conditions divided by the corresponding image taken without the test pattern to eliminate beam non-uniformity. From the figure we can see that, the thicker the SCF, the more blurred the image.

3.2. Data processing

First, we investigated the effect of the SCF's thickness on the detection efficiency. Using data from Table 2, we normalized exposure time and the value of the ionization chamber current for each objective, then the relative contribution of the 4.6 μm-thick GGG:Tb and the 20 μm-thick

GGG:Tb to the detection efficiency was calculated yielding an experimental result of about 1:3.02. As a comparison, the relative ratio of detection efficiency was obtained from the simulation methods in §2.2 yielding a result of about 1:2.26. One possible reason for the difference between the experimental and simulation results may be that the actual Tb doping concentration in two of the SCFs is different (Cecilia *et al.*, 2014) and the simulation assumes the same doping concentration.

Second, to test the effectiveness of the method for simulating the detector's best-focus PSF, the blurred images in Figs. 12(A1)–12(D1) need to be deconvolved by using the best-focus PSFs. The deconvolution algorithm used in this article is the Richardson–Lucy deconvolution (Richardson, 1972; Lucy, 1974). It is an iterative procedure for recovering a latent image that has been blurred by a known PSF. When using the simulated PSF to deconvolve the blurred image, as the number of iterations increases, the noise in the image will be amplified, and then lead to iteration results that deviate from the actual value. To reduce the impact of noise on the iterative results, we have limited the number of iterations. The method used for this is to find an area with almost uniform light intensity in the image (see the red dotted boxes in Fig. 12) and calculate the relative standard deviation of the pixels within the area. The formula for the relative standard deviation (RSD) is shown in formula (7),

$$\Delta\sigma = \frac{\left\{(1/m)\left[\sum_{i=1}^{m}(x_i - \bar{x})^2\right]\right\}^{1/2}}{\bar{x}}, \qquad (7)$$

where x_i is a single-pixel value, $\bar{x}$ is the average of the pixel values, and m is the number of pixels in the area (Gao *et al.*,
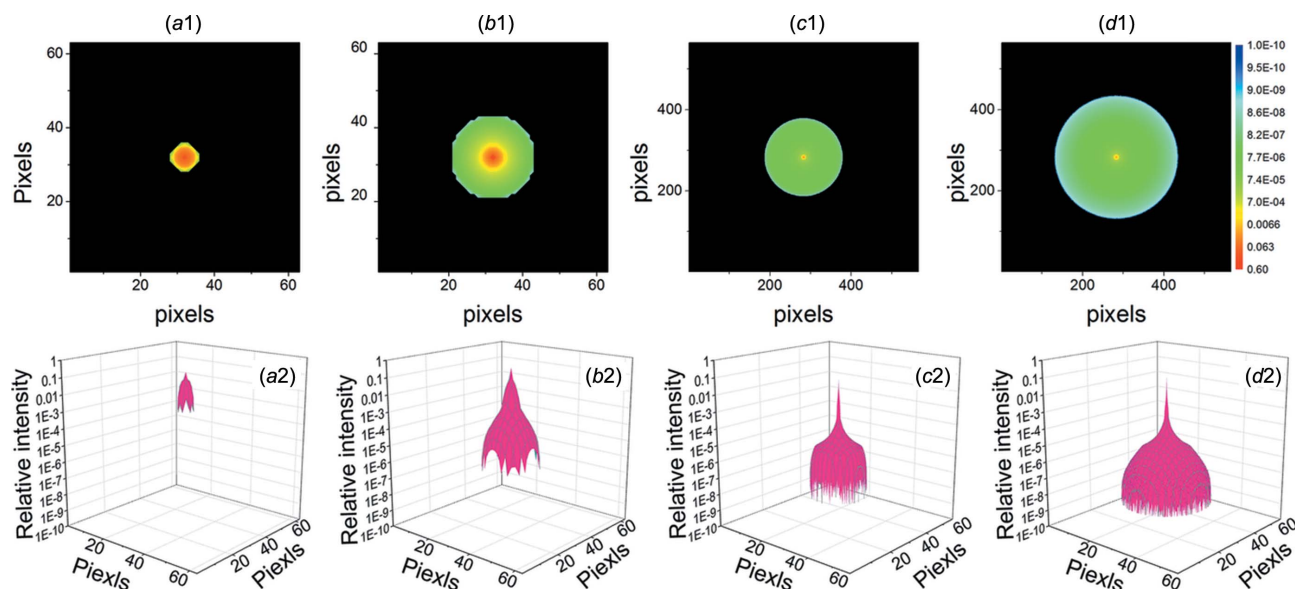

Figure 11
Sketch of the best-focus PSFs' light intensity distribution in the *XY* plane. (*a*1)–(*d*1) PSFs with pseudo-color. (*a*2)–(*d*2) PSFs with three-dimensional maps. (*a*1)–(*a*2) 10× objective and 4.6 μm-thick GGG:Tb. (*b*1)–(*b*2) 10× objective and 20 μm-thick GGG:Tb. (*c*1)–(*c*2) 40× objective and 4.6 μm-thick GGG:Tb. (*d*1)–(*d*2) 40× objective and 20 μm-thick GGG:Tb. In (*a*1)–(*b*1) and (*a*2)–(*b*2), the pixel size in object space is about 0.3939 μm, and the pixel size in (*c*1)–(*d*1) and (*c*2)–(*d*2) is about 0.0985 μm. In the figure, when the objective is the same, the thicker the SCF, the more diffuse the best-focus PSF becomes.
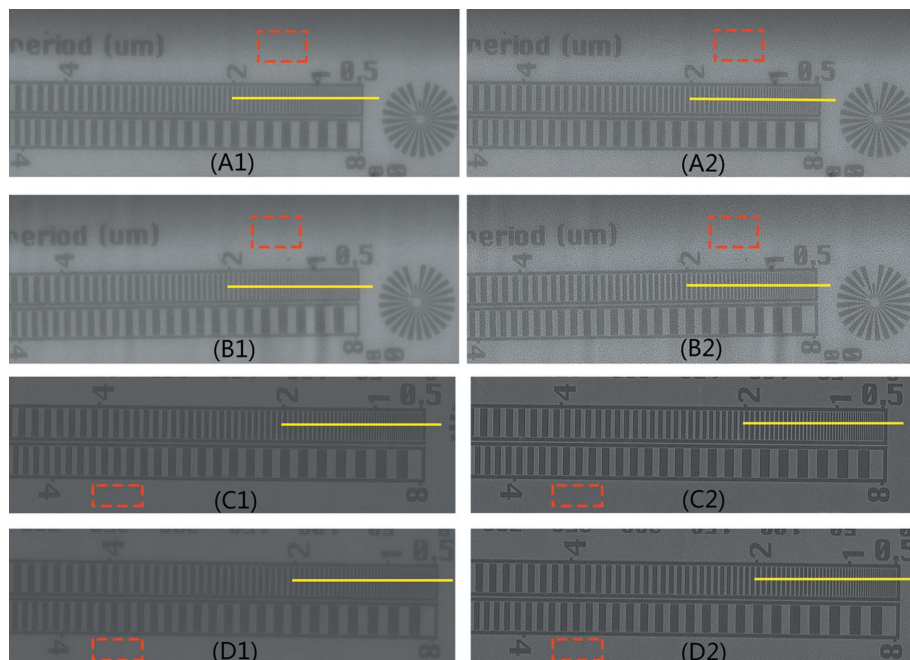
Figure 12
Comparison showing the original images and the deconvolved images. The four images on the left are original images under different conditions. The experimental conditions are: (A1) 10× objective (NA = 0.4) and 4.6 μm-thick GGG:Tb. (B1) 10× objective (NA = 0.4) and 4.6 μm-thick GGG:Tb. (C1) 40× objective (NA = 0.6) and 4.6 μm-thick GGG:Tb. (D1) 40× objective (NA = 0.6) and 20 μm-thick GGG:Tb. The four images on the right correspond to the respective PSF deconvolution results of the images on the left. To show the details more clearly, (A1), (B1), (A2) and (B2) are only part of the original image. To show the spatial frequencies from 62.5 line-pairs mm^{-1} to 1000 line-pairs mm^{-1}, (C1), (D1), (C2) and (D2) are mosaics of four original images.

the 40× objective, the number of iterations is 9× and 17× for the 4.6 μm-thick GGG:Tb and 20 μm-thick GGG:Tb, respectively. Figs. 12(A2)–12(D2) show the deconvolved images after the iteration was terminated. Comparing the images before and after deconvolution, it can be seen that the images after deconvolution become relatively clear. In order to show the changes of the contrast after deconvolution, an intensity profile along the yellow lines in Fig. 12 is plotted in Fig. 14. It can be seen that after deconvolution the contrast of the images shows a clear improvement.

Third, the spatial MTF measures the detector's ability to faithfully transmit the image contrast present in the SCF. Therefore, in order to quantitatively measure the changes in the quality of the images before and after deconvolution, the images in Fig. 12 were used to calculate the changes in the detector's MTF. The formula for the MTF is shown in formula (8),

$$\mathrm{MTF}(\nu) = \frac{\mathrm{Contrast_{image}}(\nu)}{\mathrm{Contrast_{object}}(\nu)}, \quad (8)$$

2013). When $\Delta\sigma > 0.1$, the iteration process is stopped. Fig. 13 shows the variation of $\Delta\sigma$ with the number of iterations. According to the stopping criterion, for the 10× objective, the number of iterations is 21 times and 17 times for the 4.6 μm-thick GGG:Tb and 20 μm-thick GGG:Tb, respectively. For
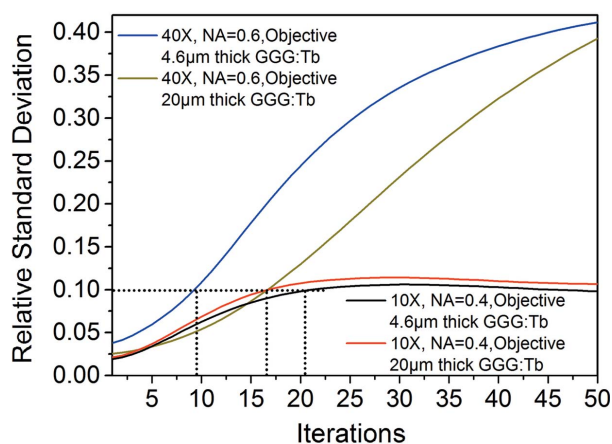
where Contrast$_{object}$(ν) is the contrast in the object space, Contrast$_{image}$(ν) is the contrast in the image space, and ν is the spatial frequency. In theory, ν should be the frequency of the sine wave and cone wave (Mochizuki et al., 1995). However, it is difficult to make a sinusoid. Therefore, in this article, the square wave's spatial frequency was taken as the spatial frequency of the sinusoidal frequency. The square wave in the Xradia resolution test pattern is made of Au with a thickness of 1.6 μm. When the 12 keV X-rays are passing through the Au film, the X-ray transmittance is about 57.386% (Henke et al., 1993). Then the contrast of all spatial frequencies in object space can be calculated as 27.076%. According to the test resolution pattern's images before and after deconvolution, the image space contrast of some frequencies can be calculated. Then, substituting the data in formula (8), the detector's MTF curves can be obtained (see Fig. 15). From Fig. 15 it can be seen that, for the original image, when the objective is the same, then the thicker the SCF, the faster that the MTF curve drops. After deconvolution of the blurred image, the MTF value of the detector is increased, but the trend of the MTF curve is different from the original MTF. For the 10× objective, the MTF curves after deconvolution first decline from 62.5 line-pairs mm^{-1} to 125 line-pairs mm^{-1}, then increase from 125 line-pairs mm^{-1} to 500 line-pairs mm^{-1} and decline again from 500 line-pairs mm^{-1} to 625 line-pairs mm^{-1}. After deconvolution for the 40× objective, the MTF curves increase from 62.5 line-pairs mm^{-1} to 500 line-pairs mm^{-1}, and

Figure 13
The relative standard deviation of the deconvolution images varies with the number of iterations. The RSD was calculated by using the values in the red box in Fig. 12. When the RSD is about 0.1, for the 10× objective, the number of iterations is 21 times and 17 times for the 4.6 μm-thick GGG:Tb and 20 μm-thick GGG:Tb, respectively. For the 40× objective, the number of iterations is 9 times and 17 times for the 4.6 μm-thick GGG:Tb and 20 μm-thick GGG:Tb, respectively.
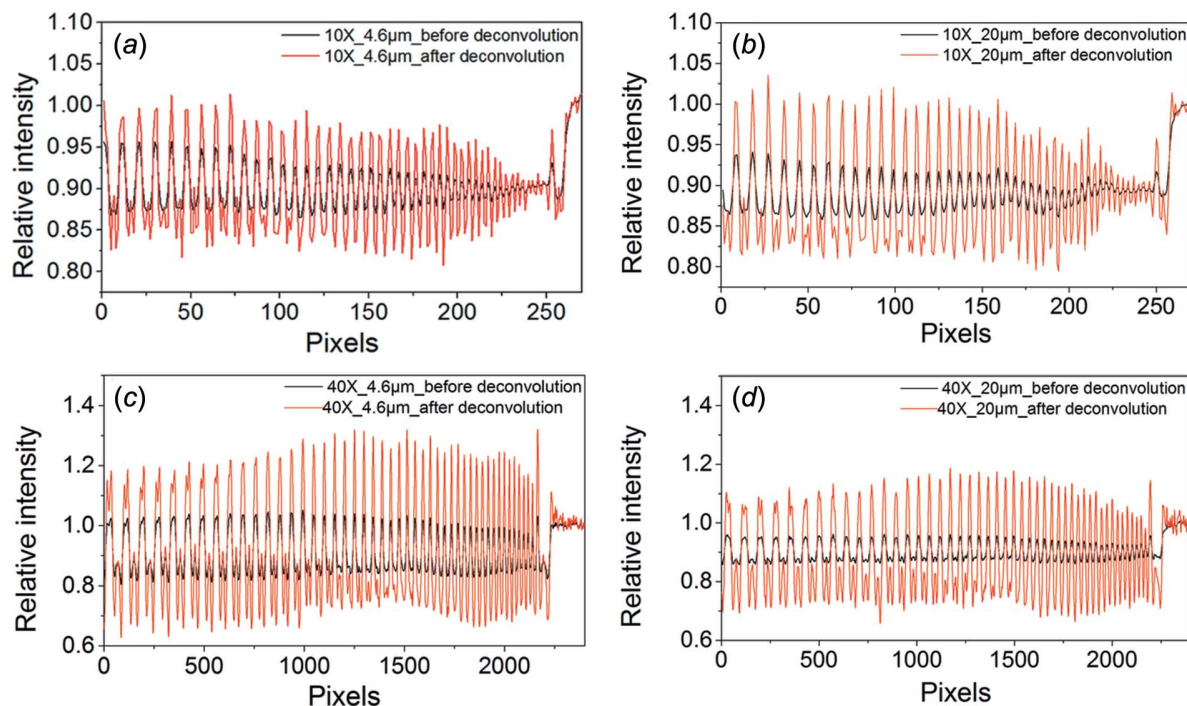
Figure 14
Comparison of the intensity profiles along the horizontal solid yellow lines in the images of Fig. 12 before and after deconvolution. It is clear that after deconvolution the contrast of the profiles has been significantly improved.
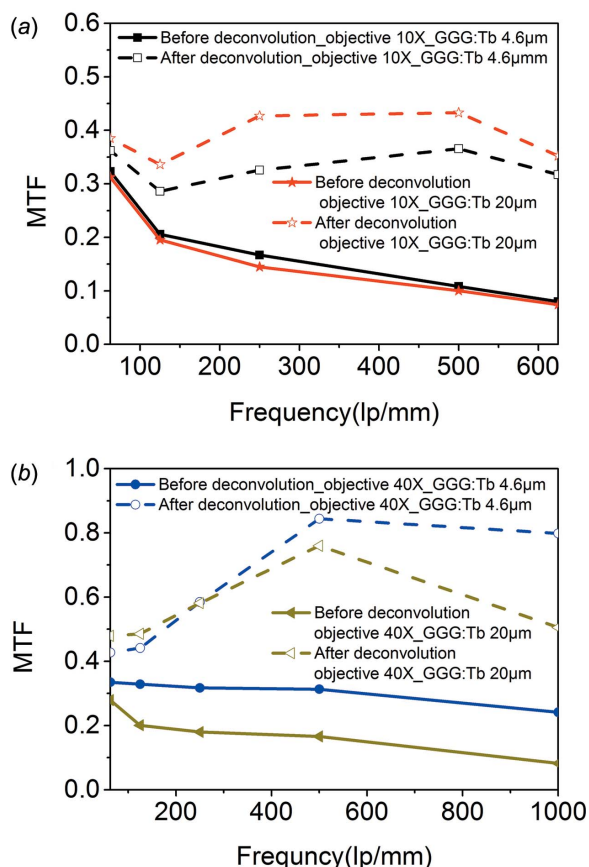

Figure 15
The changes of the MTF before and after deconvolution. It can be seen that after deconvolution the MTF had been clearly improved for both the 4.6 μm- and 20 μm-thick GGG:Tb.

decrease from 500 line-pairs mm^{-1} to 1000 line-pairs mm^{-1}. In addition, the deconvolution MTF curves with a 20 μm-thick GGG:Tb are better than the original MTF curves with a 4.6 μm-thick GGG:Tb. Therefore, after the original image was deconvolved by the simulated PSF, the detector's MTF can be improved. In that way, the thicker SCF can be used to increase detection efficiency, while still keeping the MTF of the detector at a high level.

4. Application

In order to verify whether this method is effective for general applications, dehydrated mouse brain tissue was used as a test sample and imaged at beamline 13W1 at the Shanghai Synchrotron Facility (SSRF).

In the experiment, the detector was specifically configured with 50 μm-thick LuAG:Ce, 10× objective (NA = 0.4), and sCOMS camera (HAMAMATSU, ORCA-Flash4.0) which operates with 2048 × 2048 pixels, each with a physical pixel size of 6.5 μm. After all the parts were matched together, the effective pixel size of the detector is 0.65 μm. The 12 keV X-ray energy was chosen by a Si(111) double-crystal monochromator, and the sample (mouse brain tissue) to detector (SCF) distance was about 10 cm. After finding the best focus position between the scintillation crystal and the objective lens, the mouse brain tissue projection images were captured on the CCD. For each projection image, the exposure time was 2 s. Fig. 16(a) shows one of the partially enlarged mouse brain tissue projections. We can see that the image is blurry due to the effect of the scintillation crystal thickness. From the
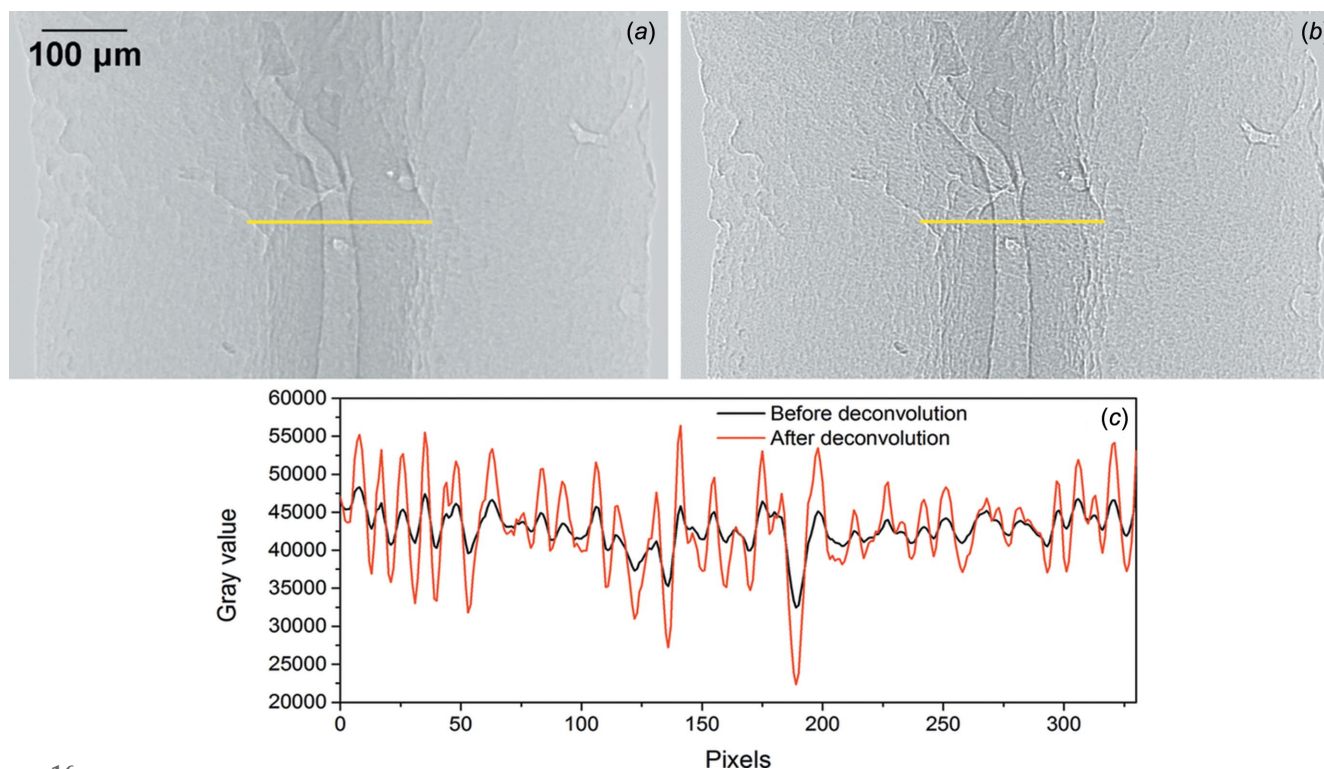
Figure 16
Image of a mouse brain tissue projection acquired with 0.65 µm effective pixel size at 13W1 (SSRF) using the BSRF detector with a 10× objective (NA = 0.4), and a 50 µm-thick LuAG:Ce scintillator. (*a*) Original image. (*b*) Deconvolved image. (*c*) Comparison of the profiles, corresponding to the horizontal yellow solid line of before and after deconvolution of the images in (*a*) and (*b*). From the profiles in (*c*), (*b*) shows more detail and provides a clearer image than (*a*).

perspective of human vision, it is difficult to see sample details. Therefore, we used our proposed method to improve the quality of the blurred images. The scintillation crystal parameters are as follows: the wavelength was taken as 535 nm which is the maximum emission wavelength of the LuAG:Ce; the corresponding refractive index for this wavelength is about 1.84. We simulated the PSFs of the detector and found the best-focus PSF using the method described in this article. Then using the PSF of the best focus position to deconvolve the original images, we obtained the deconvolution result shown in Fig. 16(*b*). It is obvious that the deconvolved image has a better image quality. In addition, we compared the profiles, corresponding to the horizontal yellow solid line before and after deconvolution of the images in Figs. 16(*a*) and Fig. 16(*b*). It can be seen that the image after deconvolution has better spatial contrast and can recover particularly minute image details. We then applied CT reconstruction methods on the original images and deconvolution images. The reconstructed results are shown in Figs. 17(*a*1) and 17(*b*1). By comparison, it can be seen that Fig. 17(*b*1) is relatively clear and details can be seen more easily. However, since the internal structure of the mouse brain tissue has a very low density, the observable contrast within the two CT slices is very poor. It has been shown that the application of the contrast stretching transformation method has been used as an image enhancement technique to improve the visibility of low-contrast images (Gonzalez & Woods, 2002). Therefore, we performed this method on the CT slices in Figs. 17(*a*1) and 17(*b*1), respec-
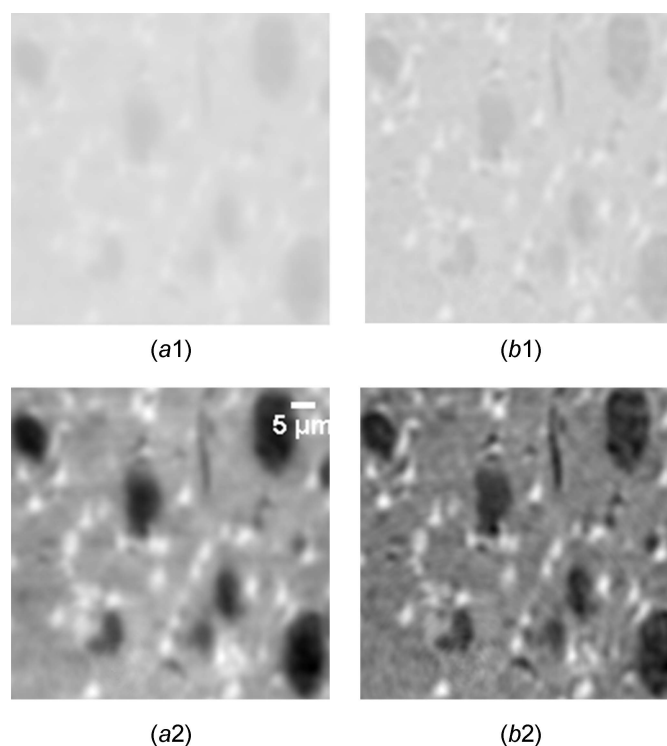

Figure 17
CT reconstruction section images of mouse brain tissue (local magnification). (*a*1) Original data reconstruction result. (*b*1) Deconvolution data recontruction result. (*a*2) and (*b*2) are the results from the contrast stretch transformation of (*a*1) and (*b*1), respectively.

tively. The corresponding results are shown in Figs. 17(*a*2) and 17(*b*2). The two images now have better contrast, but Fig. 17(*b*2) is clearer and the structural differences can be seen more easily. Therefore, we can conclude that the method in this article is effective for biological samples. This will have a very important significance for biological samples with very small differences in density. At the same time, we believe that the method in this article will be effective for samples in other fields.

5. Discussion

It should be noted that some factors are not taken into consideration in the process of simulating the PSFs of the detectors. The method to obtain the PSF is mainly based on geometrical optics. We did not take into account the diffraction of the lens system in the PSF calculation, which will result in a difference between the real PSF and our calculated results. In the simulation, we considered the X-rays to be a parallel beam; in fact the real synchrotron radiation source has a divergence of about 1 mrad, which will make PSF more diffuse. X-rays will be scattered when they penetrate into the scintillator. In our case the X-ray energy is not very high, and thus the scattering is small enough that it can be ignored. While this scattering would be more important for higher-energy X-rays, it should not be neglected in the simulation. Additionally, we take the scintillator to have a particular thickness, which may differ from the actual situation. The aberration in the lens system is also neglected in this article and that will affect the accuracy of the PSF. Therefore, the PSF simulated in this paper is only an approximation of the actual PSF.

The deconvolved image was obtained by an iterative deconvolution algorithm. Theoretically, after deconvolution, the MTF value should be close to 1, and the trend of the MTF as a function of frequency should be the same as that of the original MTF, but, as Fig. 15 shows, this is not the case. One contributing factor is that the simulated PSF is only an estimate of the PSF. Another important factor is that the deconvolution will amplify the noise, which exists at all frequencies in the image. However, we just chose a simple criterion to finish the iteration. Therefore, as Fig. 13 shows, when original images with different levels of noise are deconvolved, the criterion chosen will lead to different iteration times which will, in turn, affect the solutions of the deconvolution results. Hence it is very difficult to obtain an ideal image solution when a deconvolution algorithm is used to deconvolve images with noise (Rafael *et al.*, 2014).

In addition, as can be seen from Fig. 15(*b*), under the conditions of the 40× objective (NA = 0.6) and 4.6 μm-thick GGG:Tb, and in the frequency range between 500 line-pairs mm^{-1} and 1000 line-pairs mm^{-1}, the deconvolved MTF has grown to about 0.8 due to the fact that the original image has a relatively good quality with an MTF of about 0.3. However, under the same conditions but using the 20 μm-thick GGG:Tb, the MTF of the original image is lower and dropped to about 0.1 at a spatial frequency of 1000 line-

pairs mm^{-1}. This makes the deconvoluted MTF lower than for the case using the 4.6 μm-thick GGG:Tb. Therefore, the thickness of the SCF will affect the deconvolved MTF of the detector. According to formula (1), the DOF of the detector is about 1.53 μm. The thickness of the 4.6 μm and 20 μm scintillating crystals is 3 and 13 times the DOF, respectively. We conclude that when the thickness of the scintillation crystal is much larger than the DOF the increase in the deconvolved MTF will be lower than for a detector using a thin SCF. As to what thickness of scintillation crystal will make the image after deconvolution result in an optimal MTF, this requires conclusions based on the actual experimental conditions and deconvolution results. What is more, it is known that the thickness of the SCF is a key factor affecting the quality of the original image. When a user images a sample with small differences in density, the use of a thick SCF will overwhelm the sample details due to the fact that the MTF is too low. In that case, a relatively thin scintillation crystal should be used to ensure that the image details can be recovered. If the relative differences in the density of the sample are large, a thicker scintillation crystal can be used, and a good quality image still can be restored from the original image. That is to say, the density of the sample itself is also a key factor when choosing the thickness of the scintillation crystal to improve detection efficiency. Therefore, it is difficult to give quantitative guidelines for choosing the optimum thickness of the scintillation crystals; the users should choose the appropriate thickness of the scintillation crystal to yield the highest detection efficiency based on the density differences within the sample. For detector manufacturers, they should provide users with different thicknesses of scintillation crystals, allowing users to select SCF thickness based on the details of the sample. If the manufacturer can integrate this method into the detector, the image quality can be improved in real time, which is of great significance when a thick SCF is used to improve detection efficiency.

Based on the above discussion, in the future we will consider many factors to improve the method of simulating the detector PSF, look for ways to optimize the deconvolution algorithm in order to better suppress noise in the original images, and study the relationship between the quality of image restoration and the thickness of scintillator crystals used to improve detection efficiency.

6. Conclusion

We developed a method to obtain the PSF according to the performance parameters of the lens-coupled system based on the simulation of the imaging process. This method was applied to a hard X-ray indirect imaging detector, which was developed by BSRF. The calculated PSFs were used in the deconvolution of images from an Xradia resolution test pattern and deconvolution results under different experimental conditions were compared. The results showed that, after deconvolution, the MTF had been improved for both 4.6 μm- and 20 μm-thick GGG:Tb scintillators. Additionally, the MTF of a deconvolved image with a 20 μm-thick GGG:Tb

is higher compared with the original image with a 4.6 µm-thick GGG:Tb, and the X-ray intensity measured in the detector was about three times higher in the same exposure time. In order to show the effectiveness of the method in real samples, we performed an imaging experiment and performed our deconvolution processing on mouse brain tissue. We then reconstructed the original data and the deconvolution data separately. In addition, the contrast of the CT reconstruction results was extended using the contrast stretching transformation method. The results show that the quality of the images after application our methods are better than the original results. Therefore, the method in this article shows the promise of enabling the use of thicker SCFs to improve detector efficiency while keeping a high MTF.

References

Ajoy, G. (2008). *Optics*, ch. 5, 7–10. Tsinghua University Press.

Bamieh, B., Paganini, F. & Dahleh, M. A. (2002). *IEEE Trans. Autom. Contrib.* **47**, 1091–1107.

Bebek, C. J., Coles, R. A., Denes, P., Dion, F., Emes, J. H., Frost, R., Groom, D. E., Groulx, R., Haque, S., Holland, S. E., Karcher, A., Kolbe, W. F., Lee, J. S., Palaio, N. P., Roe, N. A., Tran, C. H. & Wang, G. (2012). *Proc. SPIE*, **8453**, 845305.

Bebek, C. J., Emes, J. H., Groom, D. E., Haque, S., Holland, S. E., Jelinsky, P. N., Karcher, A., Kolbe, W. F., Lee, J. S., Palaio, N. P., Schlegel, D. J., Wang, G., Groulx, R., Frost, R., Estrada, J. & Bonati, M. (2017). *J. Instrum.* **12**, C04018.

Cecilia, A., Jary, V., Nikl, M., Mihokova, E., Hänschke, D., Hamann, E., Douissard, P. A., Rack, A., Martin, T., Krause, B., Grigorievc, D., Baumbach, T. & Fiederle, M. (2014). *Radiat. Meas.* **62**, 28–34.

Cecilia, A., Rack, A., Douissard, P. A., Martin, T., dos Santos Rolo, T., Vagovič, P., Hamann, E., van de Kamp, T., Riedel, A., Fiederle, M. & Baumbach, T. (2011). *Nucl. Instrum. Methods Phys. Res. A*, **648**, S321–S323.

Douissard, P.-A., Cecilia, A., Martin, T., Chevalier, V., Couchaud, M., Baumbach, T., Dupré, K., Kühbacher, M. & Rack, A. (2010). *J. Synchrotron Rad.* **17**, 571–583.

Gao, Y. J., Ierapetritou, M. G. & Muzzio, F. J. (2013). *J. Pharm. Innov.* **8**, 72–82.

Gonzalez, R. & Woods, R. (2002). *Digital Image Processing*, 2nd ed. Englewood Cliffs: Prentice Hall.

Gruner, S. M. (2012). *Phys. Today*, **65**, 29–34.

He, Y. Q. & Guan, T. L. (1985). *Chin. Sci. Bull.* **01**, 14–15.

Henke, B. L., Gullikson, E. M. & Davis, J. C. (1993). *At. Data Nucl. Data Tables*, **54**, 181–342.

Hoheisel, M., Giersch, J. & Bernhardt, P. (2004). *Nucl. Instrum. Methods Phys. Res. A*, **531**, 75–81.

Kenneth, R. S. & Michael, W. D. (2017). *Depth of field and depth of focus*, https://www.microscopyu.com/microscopy-basics/depth-of-field-and-depth-of-focus.

Khartsev, S. I. & Grishin, A. M. (2005a). *Appl. Phys. Lett.* **86**, 141108.

Khartsev, S. I. & Grishin, A. M. (2005b). *Appl. Phys. Lett.* **87**, 122504.

Koch, A., Raven, C., Spanne, P. & Snigirev, A. (1998). *J. Opt. Soc. Am. A*, **15**, 1940–1951.

Li, G., Chen, C. H., Chen, Y. N., Chang, C. H. & Tsai, K. H. (2015). *Biomed. Eng. Online*, **14**, 14.

Lucy, L. B. (1974). *Astron. J.* **79**, 745–754.

McKetty, M. H. (1998). *Radiographics*, **18**, 151–163.

Manoochehri, F. & Ikonen, E. (1995). *Appl. Opt.* **34**, 3686–3692.

Martin, T., Douissard, P. A., Couchaud, M., Cecilia, A., Baumbach, T., Dupre, K. & Rack, A. (2009). *IEEE Trans. Nucl. Sci.* **56**, 1412–1418.

Martin, T., Douissard, P. A. & Mathieu, E. (2010). *Thin-film scintillators*, http://www.esrf.eu/files/live/sites/www/files/Industry/documentation/F2_Scintillators.pdf.

Martin, T. & Koch, A. (2006). *J. Synchrotron Rad.* **13**, 180–194.

Mochizuki, T., Zhang, X. W., Sugiyama, H., Zhao, J. Y., Ando, M. & Yoda, Y. (1995). *Rev. Sci. Instrum.* **66**, 2167–2170.

Rafael, C. G., Richard, E. W. & Steven, L. E. (2014). *Digital Image Processing using MATLAB*, 2nd ed., pp. 79–102. Upper Saddle River: Prentice-Hall.

Rahmani, S., Mohammadi Nia, M., Akbarzadeh Baghban, A., Nazari, M. R. & Ghassemi-Broumand, M. (2014). *Contact Lens Anterior Eye*, **37**, 451–454.

Richardson, W. H. (1972). *J. Opt. Soc. Am.* **62**, 55–59.

Smith, G. E. (2011). *J. Appl. Phys.* **109**, 6.

Uesugi, K., Hoshino, M. & Yagi, N. (2011). *J. Synchrotron Rad.* **18**, 217–223.

Wang, Q., Zhu, Y. N. & Li, H. W. (2015). *Opt. Express*, **23**, 33753–33776.

Yi, Q., Li, G., Zhang, J., Luo, S.-N., Fan, D., Gao, Z., Wang, Y., Gao, G., Jiang, S. & Jiang, X. (2015). *J. Synchrotron Rad.* **22**, 1062–1071.

Yuan, Q. X., ZHU, P. P., Huang, W. X., Wang, J. Y., Wu, Z. Y. & Hu, T. D. (2007). *Nucl. Tech.* **30**, 8.

Zorenko, Y., Gorbenko, V., Nikl, M., Mares, J. A., Martin, T. & Douissard, P. A. (2010). *IEEE Trans. Nucl. Sci.* **57**, 1335–1342.

Zorenko, Y., Gorbenko, V., Savchyn, V., Zorenko, T., Grinyov, B., Sidletskiy, O. & Fedorov, A. (2014). *J. Cryst. Growth*, **401**, 577–583.